1-1-2015

Brittle versus ductile behaviour of nanotwinned copper: A molecular dynamics study

Linqing Pei
University of Wollongong, lp115@uowmail.edu.au

Cheng Lu
University of Wollongong, chenglu@uow.edu.au

Xing Zhao
University of Wollongong, xz920@uowmail.edu.au

Liang Zhang
University of Wollongong, lz592@uowmail.edu.au

Kuiyu Cheng
University of Wollongong, kc938@uowmail.edu.au

See next page for additional authors

Brittle versus ductile behaviour of nanotwinned copper: A molecular dynamics study

Abstract

Nanotwinned copper (Cu) exhibits an unusual combination of ultra-high yield strength and high ductility. A brittle-to-ductile transition was previously experimentally observed in nanotwinned Cu despite Cu being an intrinsically ductile metal. However, the atomic mechanisms responsible for brittle fracture and ductile fracture in nanotwinned Cu are still not clear. In this study, molecular dynamics (MD) simulations at different temperatures have been performed to investigate the fracture behaviour of a nanotwinned Cu specimen with a single-edge-notched crack whose surface coincides with a twin boundary. Three temperature ranges are identified, indicative of distinct fracture regimes, under tensile straining perpendicular to the twin boundary. Below 1.1 K, the crack propagates in a brittle fashion. Between 2 K and 30 K a dynamic brittle-to-ductile transition is observed. Above 40 K the crack propagates in a ductile mode. A detailed analysis has been carried out to understand the atomic fracture mechanism in each fracture regime.

Keywords

ductile, molecular, versus, copper, brittle, nanotwinned, dynamics, behaviour, study

Disciplines

Engineering | Science and Technology Studies

Publication Details

Pei, L., Lu, C., Zhao, X., Zhang, L., Cheng, K., Michal, G. & Tieu, K. (2015). Brittle versus ductile behaviour of nanotwinned copper: A molecular dynamics study. Acta Materialia, 89 1-13.

Authors

Linqing Pei, Cheng Lu, Xing Zhao, Liang Zhang, Kuiyu Cheng, Guillaume Michal, and A Kiet Tieu

Brittle versus ductile behaviour of nanotwinned copper: A molecular dynamics study

Linqing Pei[1], Cheng Lu[1*], Xing Zhao[1], Liang Zhang[1], Kuiyu Cheng[1], Guillaume Michal[1] and Kiet Tieu[1]

[1] School of Mechanical, Materials and Mechatronic Engineering, University of Wollongong, Wollongong, NSW 2522, Australia

*Corresponding author. Tel.:+6142214639; fax: +61242213101; E-mail address: chenglu@uow.edu.au (C. Lu)

Abstract

Nanotwinned Copper (Cu) exhibits an unusual combination of ultra-high yield strength and high ductility. A brittle-to-ductile transition was previously experimentally observed in nanotwinned Cu despite Cu being an intrinsically ductile metal. However, the atomic mechanisms responsible for brittle fracture and ductile fracture in nanotwinned Cu are still not clear. In this study, Molecular Dynamics (MD) simulations at different temperatures have been performed to investigate the fracture behaviour of a nanotwinned Cu specimen with a single-edge-notched crack whose surface coincides with a twin boundary. Three temperature ranges are identified, indicative of distinct fracture regimes, under tensile straining perpendicular to the twin boundary. Below 1.1 K, the crack propagates in a brittle fashion. Between 2 K and 30 K a dynamic brittle-to-ductile transition is observed. Above 40 K the crack propagates in a ductile mode. A detailed analysis has been carried out to understand the atomic fracture mechanism in each fracture regime.

Keywords: Molecular dynamics; Nanotwinned Cu; Fracture

1. Introduction

The fracture of a material is usually categorised into brittle fracture and ductile fracture. A brittle fracture propagates along a crystallographic plane by cleavage due to high stress concentration at the crack tip. A ductile fracture is accompanied by plastic deformation characterised by dislocation nucleation and dislocation mobility [1]. Transition from brittle to ductile fracture has been observed in a range of materials over different temperature ranges. The accepted mechanism governing the brittle-to-ductile transition is the competition between loss of inter-atomic bonds and dislocation process at or near the crack tip [2-6]. The study of the atomic-scale fracture process around the crack tip is a central issue in understanding fracture ductility, fracture embrittlement and the associated transition regime in materials having different microstructures.

Rice and Thomson [3], followed by Anderson and Rice [7] and Li [8], compared the brittle and ductile fracture response on the basis of the energy competition between propagation of a Griffith cleavage and a dislocation nucleated at a crack tip. When the energy release rate associated with the emission of a single dislocation was less than the Griffith cleavage energy, it was assumed that a dislocation would be spontaneously emitted before cleavage, and vice versa. Rice [5] used the ratio of surface energy to the unstable stacking fault energy to predict the brittle and ductile response of Face Centred Cubic (FCC) and Body Centred Cubic (BCC) metals. Zhou and Thomson [9] proposed that ledges on cracks could be efficient sources for dislocation emission at loads well below the critical load. The dislocations could be more easily emitted compared to homogenous dislocations because of the existing finite lengths of dislocations at the ledge. Freund and Hutchinson [10] found that the brittle-to-ductile transition could be determined by the crack's ability to overrun the active plastic zones. As pointed out by Argon [11], it is possible to nucleate dislocations from the tip of a propagating cleavage crack at finite temperatures in many intrinsically brittle solids. While the cleavage process at the crack tip is primarily independent of temperature, the initiation of dislocation

loops from the crack tip can be significantly assisted by thermal activation. At a given temperature, and at a crack velocity below a critical value, more dislocation emissions from the crack tip lower the crack tip stress below the level necessary for continued cleavage, resulting in a brittle-to-ductile transition.

Atomistic simulations have been widely used to examine fracture propagation in solids. Knap and Sieradzki [12] conducted Molecular Dynamics (MD) simulations for FCC solids subjected to Mode I and Mode II loadings. Their observations of dislocation nucleation from Mode II fracture simulations were in reasonably good agreement with Rice's prediction [5]. In Mode I, Rice's continuum formulation underestimated the stress intensity for dislocation emission by almost a factor of 2 compared to the MD results. Cleri et al. [13] reported that the Burgers vectors of the straight edge dislocations nucleated from the crack tip and the slip plane inclination with respect to the crack plane observed in atomistic simulations were consistent with the predictions of the continuum elasticity theory. However, they suggested that the unstable-stacking energy in Rice's formulation, which was based on the concept of a homogeneous displacement field, should be replaced by a suitably defined energy barrier for dislocation nucleation that fully incorporates the displacement inhomogeneity in the vicinity of the nucleating dislocation. Abraham and Gao [14] found from MD simulations that the FCC crystal failed by brittle cleavage for cracking on a {110} plane growing in the [110] direction and by ductile plasticity for cracking on a {111} plane growing in the [110] direction. Comparison of equilibrium surface energies on the crack plane and Schmid factors on the primary slip systems indicated that the classical theories of fracture gave predictions in contradiction with the simulation results. A hyper-elasticity model was proposed by Abraham and Gao [14] to explain this discrepancy. It has also been found that if the speed of the (110) brittle crack reached approximately one-third of the Rayleigh sound speed, a dynamic brittle-to-ductile transition occurred [15]. Zhang et al. [16] reported that the geometry of the crack

and crystal orientations had a strong effect on the processes at the crack tip. Kimizuka et al. [17] studied the dynamic behaviour of dislocations near a crack tip in FCC metals. Results obtained for copper and aluminium showed multiple emissions of dislocation loops from the crack tip and incipient evolution of plastic deformation during crack extension. Cui and Beom [18] investigated single Cu and Al crystals with edge cracks under Mode I loading conditions using MD simulations. In their simulation model a crack with its front along the [011] direction was inserted on the (100) plane. Five different crack lengths were employed to examine the effect of crack length on the fracture behaviour of each material. The results indicated that Cu and Al exhibited different fracture mechanisms. The above literature review shows that most investigations on brittle versus ductile behaviour using MD simulations were carried out on single crystals.

Nanotwinned Cu is a relatively new material with special microstructure. It has been the subject of intensive research due to its unusual combination of ultrahigh yield strength and high ductility [19-21]. The high ductility of nanotwinned Cu has been attributed to the gradual loss of coherency of the Twinning Boundaries (TB) during plastic deformation [22-24]. A brittle-to-ductile transition was experimentally observed in nanotwinned Cu despite Cu being an intrinsically ductile metal. Jang et al. [21] conducted *in situ* Scanning Electron Microscope (SEM) uniaxial tension tests on nanotwinned Cu nanopillars with different twin boundary orientations and twin boundary spacings. The nanopillars with twin boundary spacings up to 2.8 nm exhibited the characteristics of ductile fracture clearly, while those with the larger twin boundary spacing of 4.3 nm failed in a brittle fashion. Jang et al. [21] also performed MD simulations of crack propagation along a twin boundary in nanotwinned Cu to understand the distinct fracture modes observed in their experiments. It was found that when the twin boundaries were spaced sufficiently closely, the high stresses at the crack tip could induce twinning dislocation nucleation and propagation on the twin boundaries in close

proximity to the crack tip, leading to a cascade of dislocation activities and eventually ductile failure.

The intriguing findings of the TB-spacing-induced brittle-to-ductile transition in nanotwinned Cu from Jang et al.'s work raises some fundamental questions: 1) can the brittle-to-ductile transition be observed in this material when the temperature varies and 2) what is the atomic mechanism responsible for nucleation and mobility of dislocations emitted from the crack tip? In this paper, we explore these questions for nanotwinned Cu with a pre-existing edge-notched crack using MD simulations at various temperatures.

2. Molecular dynamics simulation model

Molecular Dynamics (MD) simulations were performed with the open-source code Large-scale Atomic/Molecular Massively Parallel Simulator (LAMMPS) [25]. The MD domain of this study is illustrated in Fig. 1. The domain is 496 Å × 501 Å × 25.16 Å in the X, Y and Z directions respectively. It was filled with Cu atoms arranged in an FCC structure. The original crystal, referred to as the matrix crystal in the following, was aligned along the $[1\ \bar{1}\ \bar{2}]$, $[\bar{1}\ 1\ \bar{1}]$ and [1 1 0] crystallographic directions in the X, Y and Z directions respectively. A set of the twinned crystals, labelled T_1-T_6 in Fig. 1, was then introduced by rotating the matrix crystal along its X axis by 180^o. This resulted in a set of separated matrix crystals, labelled M_1-M_6. The twinned crystals had crystallographic directions $[1\ \bar{1}\ \bar{2}]$, $[1\ \bar{1}\ 1]$ and $[\bar{1}\ \bar{1}\ 0]$ in the X, Y and Z directions respectively. All the crystals (T_1-T_6 and M_1-M_6) had the same height of 4.17 nm along the Y direction. In Fig. 1, the dark blue spheres are atoms with perfect FCC structures and light blue spheres are atoms at the Twin Boundary (TB). The coherent TBs between the matrix crystals and the adjacent twinned crystals are marked by light blue colour. A through-thickness crack was created by removing a number of atoms in the middle of the left-hand edge of the simulation cell as shown in Fig. 1. The crack surface was parallel to the TB plane between the T_3 crystal and the M_4 crystal. The crack front was

oriented along the Z direction. The initial length of the crack was about 65 Å. A detail of the crack tip region is given in the top-right corner of Fig. 1. The atoms surrounding the crack are coloured red. The simulation cell encapsulates over half a million atoms.

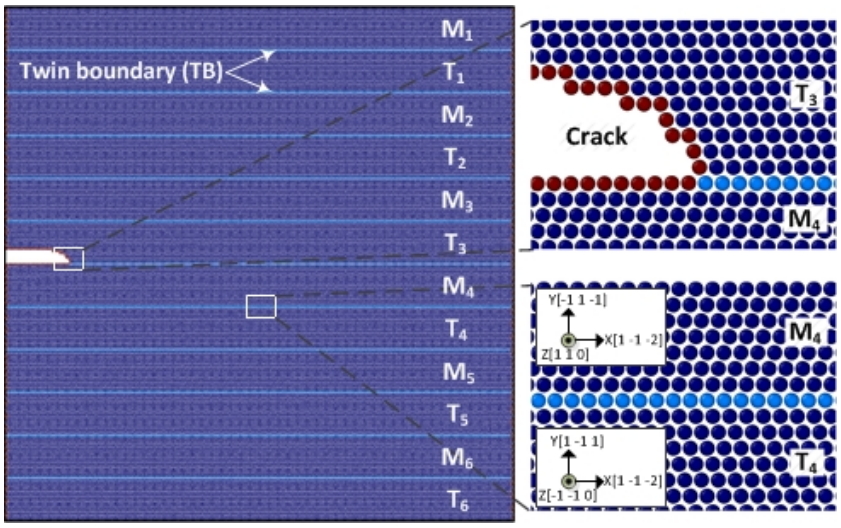

Fig. 1 Simulation domain of nanotwinned Cu with a single-edge-notched crack.

The Embedded Atom Method (EAM) interatomic potential developed by Mishin et al. [26] was employed in all the simulations. This potential was calibrated using experimental and *ab initio* data for Cu. It has been shown to precisely predict the lattice properties, point and extended defects, various structural energies and transformation paths [26]. The simulations were conducted in a constant NPT ensemble (fixed number of atoms (N), constant pressure (P) and constant temperature (T)). Periodic boundary conditions were applied in the Y and Z directions and free boundary conditions were used in the X direction. In each simulation, random velocities were initially assigned to atoms, followed by a relaxation process for 10^5 time steps. The simulation cell was subsequently stretched at a constant strain rate of 1×10^8 s^{-1} along the Y direction while the normal stress along the Z direction was fixed to zero using the Parinello-Rahman barostat. The equations of the atomic motion were integrated using the velocity Verlet algorithm. The total simulation time was 702 ps with a time step of 0.003 ps, leading to a total strain of 7.02% along the Y direction. 10 simulation cases at temperatures

(0.5 K, 1.1 K, 2 K, 5 K, 10 K, 20 K, 30 K, 40 K, 50 K and 60 K) were conducted. In each simulation the temperature was maintained using the Nose-Hoover thermostat. The Ovito software [27] was used to visualise the atomic configuration. The Crystal Analysis (CA) tool [28] and Dislocation Extraction Algorithm (DXA) code [29] developed by Stukowski and his co-workers were used to identify dislocations and stacking faults respectively. The results were viewed using the ParaView software.

3. Results

3.1 Stress-strain relation

Fig. 2 shows the normal stress along the Y direction ($\bar{\sigma}_y$) averaged over all the atoms as a function of the imposed strain (ε) for 7 simulation cases. The results of the other three cases (5 K, 20 K and 50 K) are not included because they were very similar to the presented cases. The stress components were calculated using the expression taken from the Virial theorem, and the average atom volume was used in the stress calculations [25]. The strain (ε) was calculated from the applied strain rate multiplied by the deformation time. It can be seen from Fig. 2 that all the simulation cases have a nearly-linear stress-strain relationship up to a strain of 2.52% with a tangent modulus of about 181 GPa, close to the elastic modulus of 191 GPa for pure copper along the [111] direction [30]. The difference between two values is due to existence of the edge crack.

After the strain exceeds 2.52%, all the curves drop in Fig. 2. The simulation results at 0.5 K and 1.1 K are almost identical. They drop to near-zero stress at about ε = 3.12% and then oscillate as the strain increases further. At 2 K, 10 K and 30 K, the stress does not reduce to zero. Instead, the stress drop stops at strains of 2.92%, 2.82% and 2.82% respectively. Subsequently $\bar{\sigma}_y$ increases slightly with increasing strain. In comparison, the cases at 40 K and 60 K indicate a slight stress decrease at ε = 2.52%, immediately followed by a significant

stress increase with increasing strain. The tangent modulus at 60 K is larger than that at 40 K for strains greater than 2.52%.

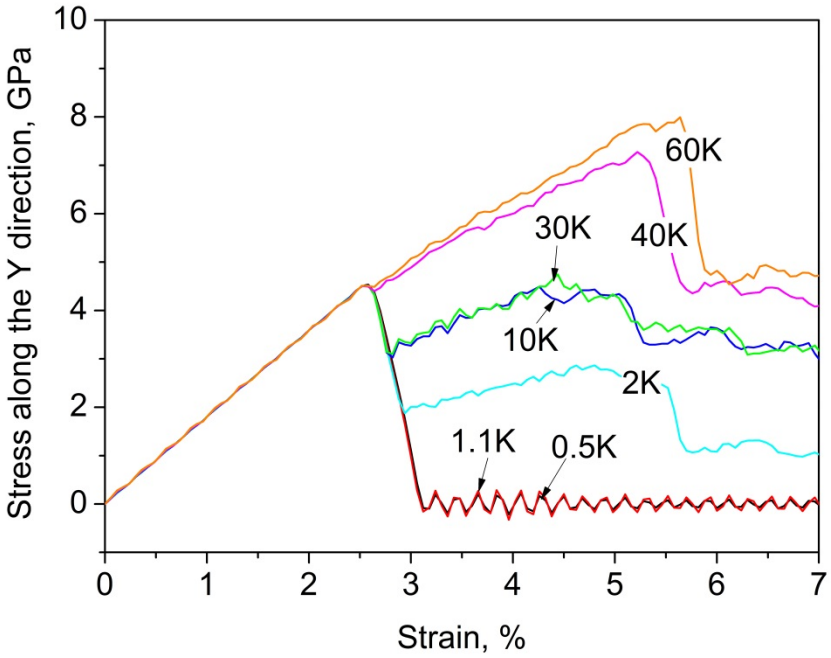

Fig. 2 Average normal stress along the Y direction as a function of the imposed strain for different simulation cases.

Three stages of the crack propagation process at 1.1 K are shown in Fig. 3. The onset of crack propagation is found at ε = 2.52%, corresponding to the peak of the stress-strain curve in Fig. 2. Crack propagation takes place at the TB between the T_3 crystal and the M_4 crystal, as shown in Fig. 3(a). In Fig. 3(b) the crack continues to propagate along the TB in a straight line as the imposed strain increases to 2.733%. The crack leaves a smooth cleavage surface in its wake. The atomic bonds break continuously during the propagation of the crack. This will release the stress on all the atoms located on the left-hand side of the crack and in turn reduce the average stress of the system, leading to the lower $\bar{\sigma}_y$ observed in Fig. 2. No dislocation has been observed in this case, implying that the crack is brittle. The crack travels through the whole simulation cell along the X direction at ε = 3.12% (Fig. 3(c)), resulting in near-zero stress observed in Fig. 2.

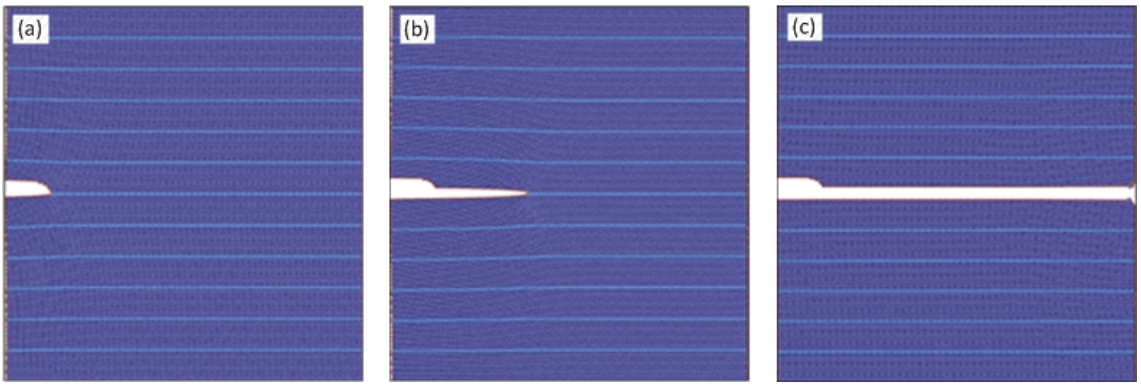

Fig. 3 Snapshots of the simulation domain subjected to different strains at 1.1 K: (a) ε = 2.52%; (b) ε = 2.733%; (c) ε = 3.12%.

3.2 Crack length

Fig. 4 shows a sequence of atomic configurations around the crack tip for a small strain range from 2.741% to 2.744% at 1.1 K. It can be seen in Fig. 3 that during the crack propagation, two adjacent planes perpendicular to the Y direction separate to move the crack tip forward. This means that the normal stress along the Y direction (σ_y) plays an important role. The colour assigned to each atom in Fig. 4 represents the magnitude of σ_y. Eight atoms near the crack tip are selected for analysis. Group-A atoms, marked A_1, A_2 and A_3 and A_4, are located on a plane above the TB, while the other four atoms (Group-B), labelled B_1, B_2, B_3 and B_4, are exactly at the TB. Fig. 4(a) corresponds to the imposed strain of 2.741%. It can be seen that a high stress region exists near the crack tip and the highest value of σ_y is associated with the atom in front of the crack tip. Atom B_1 has the highest σ_y in Fig. 4(a).

As the imposed strain increases to ε = 2.743%, Atom A_1 moves up and Atom B_1 moves down, as shown in Fig. 4(b). The distance between A_1 and B_1 and the distance between B_1 and A_2 increase significantly and the position of the maximum σ_y transfers to Atom A_2. This indicates that the crack tip has moved. As the imposed strain increases further to ε = 2.744%, as shown in Fig. 4(c), Atom B_2 has the largest σ_y.

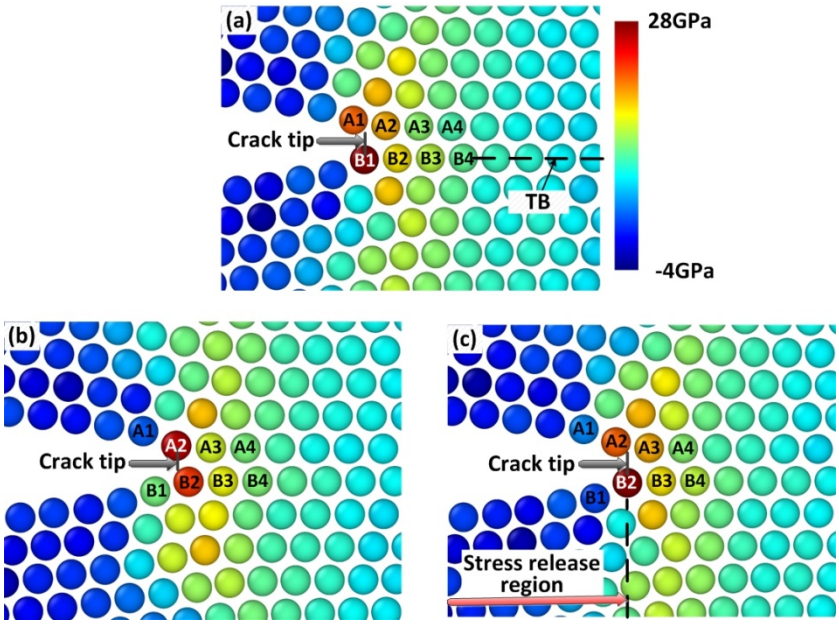

Fig. 4 Sequence of atomic configurations around the crack tip at 1.1 K: (a) ε = 2.741%; (b) ε = 2.743%; (c) ε = 2.744%.

Fig. 5(a) plots σ_y as a function of the imposed strain for the eight selected atoms. All the curves exhibit a similar pattern: σ_y increases initially with increasing strain and then decreases after it reaches a peak value. It is obvious that the peak stresses of Group-B atoms are higher than those of Group-A atoms. The curves corresponding to two neighbouring atoms intersect at a certain point. For instance, Atom A_1 and Atom B_1 have an intersection point (Point I_1) at a strain of 2.7412%, as shown in Fig. 5(a). To the left of Point I_1, Atom A_1 has a higher σ_y value than Atom B_1, while the stress for Atom B_1 exceeds that for Atom A_1 after Point I_1. Atom B_1 has its maximum stress value at ε = 2.7417% and soon afterwards its σ_y decreases with the strain. Atom A_2, another neighbour of Atom B_1, is subjected to a continuously increased σ_y during this period. Curves of Atom B_1 and Atom A_2 interact at Point I_2. It is clear in Fig. 5(a) that Atom B_1 has the highest σ_y over all the atoms between Point I_1 and Point I_2. As observed in Fig. 4 the atom with the highest σ_y is always located in front of the crack tip. Therefore, such an atom defines the location of the crack tip in this study.

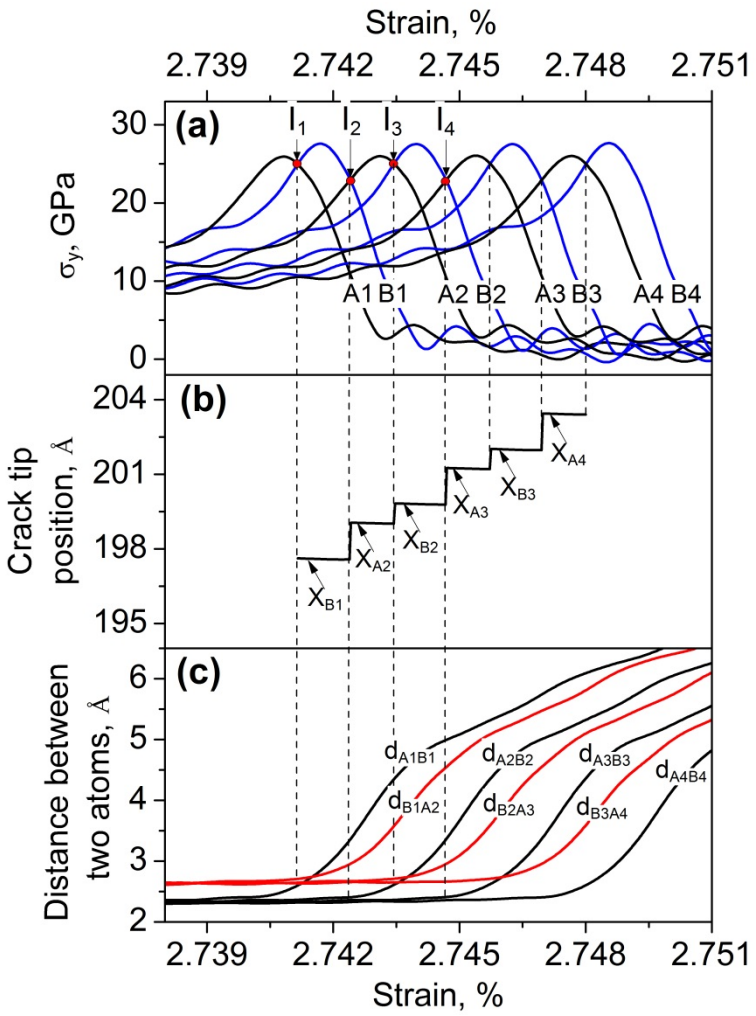

Fig. 5 Simulation results for selected atoms at 1.1 K: (a) σ_y; (b) Crack tip position; (c) Distance between a Group-A atom and a Group-B atom.

Fig. 5(b) plots the crack position, which is equal to the crack length, as a function of the imposed strain based on the results of Fig. 5(a). Between Point I_1 and Point I_2, Atom B_1 has the highest σ_y. Therefore, the crack tip is located at X_{B1}, the X coordinate of Atom B_1. Similarly the crack tip is located at Atom A_2 (X_{A2}) during the strain range between Point I_2 and Point I_3. Using this approach the crack tip position has been automatically determined by post-processing the simulation data. It is noted that this approach is only suitable for the brittle fracture propagation. Once a dislocation nucleates around the crack tip, the highest σ_y is not associated with the atom at the crack tip.

Fig. 5(c) shows the distances between Group-A atoms and Group-B atoms. The symbol ‘d’ in the figure means the distance between two atoms and its subscript consists of the names of two linked atoms. For instance, d_{A1B1} stands for the distance between Atom A_1 and Atom B_1. It is known from Fig. 5(a) that from Point I_1 to Point I_2, Atom B_1 has the highest σ_y, implying that the crack tip has moved to this atom. It is interesting to see that the distance between Atom B_1 and Atom A_2 starts to increase at Point I_1. This may indicate that the stretching of the B_1-A_2 bond is driven by Atom B_1. This conclusion also applies to the other atomic bonds (such as A_2-B_2, B_2-A_3 and A_3-B_3 as shown in Fig. 5(c)). The first-mentioned atoms in the bond names are always the ‘driving’ atoms.

3.3 Brittle-to-ductile transition

Fig. 6 shows the crack length as a function of the imposed strain for four different cases (1.1 K, 2 K, 10 K and 40 K). The solid lines and the dashed lines represent the results of brittle fracture and ductile fracture, respectively. The data in Fig. 6 was recorded for every 20 simulation steps. Only within a very small strain range simulation data was saved for every single simulation step to give detailed analysis as shown in Fig. 5. The 1.1 K case exhibits brittle fracture behaviour for the entire simulation. The cases of 2 K and 10 K have shown a dynamic brittle-to-ductile transition: the fracture first propagates in a brittle mode and then transfers to a ductile mode at a critical strain. The critical strains in the 2 K and 10 K cases are different. For the 40 K case, the fracture only moves by a very short distance in a brittle fashion and then stops its movement due to emission of a dislocation.

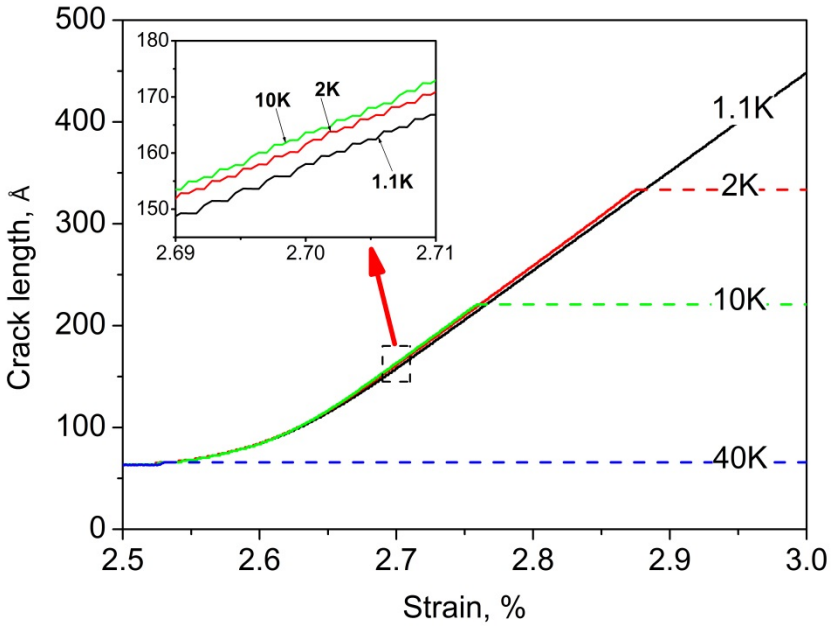

Fig. 6 Crack length as a function of the imposed strain.

All the 1.1 K, 2 K and 10 K cases exhibit a certain period of brittle crack propagation. As shown in Fig. 6 the solid curves corresponding to these cases almost overlap. The crack length increases slowly initially until the slope of the curves increases gradually with the imposed strain. The slope of the solid lines remains nearly constant after a strain of about 2.66%. Since the slope of the curve represents the crack propagation speed, Fig. 6 indicates that the speed of brittle crack propagation increases from zero with the strain and reaches a saturation value at $\varepsilon = 2.66\%$. When a brittle crack undergoes transition to a ductile fracture, the crack speed suddenly drops.

The change in crack length at 1.1 K, 2 K and 10 K is not significant. However, the inset in Fig. 6 shows that the brittle crack travels faster at higher temperature. The average crack propagation speed (v) (average slope of the solid curves) for the strain range of 2.69% ~ 2.75% is 957.1 m/s, 969.2 m/s and 978.6 m/s for the 1.1 K, 2 K and 10 K cases, respectively. Continuum fracture theory typically assumes that crack can accelerate to a limiting speed equal to the Rayleigh sound speed of the material [31]. The Rayleigh speed (c_R) can be calculated by $c_R = 0.93\sqrt{\mu/\rho}$ [32], where μ is the shear modulus and ρ is the material

density. If we choose μ = 45.2 GPa and ρ = 8931 kg/m^3 for copper [33], it yields c_R = 2092 m/s. Therefore, the propagation speed of the brittle crack observed in this study is about 45.7% ~ 46.7% of the Rayleigh speed. This is consistent with findings in experiments [34, 35] and MD simulations [15, 36], which indicated that brittle cracks have limiting velocities well below predictions by continuum fracture theory.

From the above analysis, it appears that the brittle crack propagation speed increases with temperature. This implies that brittle crack propagation is a thermally activated process. According to transition state theory [37], the activation energy barrier (Q) for the brittle crack propagation can be expressed by the equation $v = v_0 \exp(-Q/(k_B T))$, where v is the brittle crack propagation speed, v_0 is a reference speed, k_B is the Boltzmann constant and T is the temperature. Q can be determined by regression of this equation using the speeds at three temperatures obtained before. The calculated activation energy is 0.11 eV. Zhu et al. [23] conducted atomistic modelling to investigate the dislocation/TB interaction in a twinned Cu bicrystal. In their simulations a perfect screw dislocation was driven toward the TB by a shear stress. Two competing pathways were identified. The first path was a two-step process involving the absorption of the incoming screw dislocation into the TB, followed by desorption. The second pathway involved direct transmission of the incoming screw dislocation by cross slip. The activation energies calculated from the Zhu et al.'s simulations were 0.49 eV for the absorption process and 0.67 eV for the direct transmission process, respectively. The activation energy for the desorption process was much higher, approximately 5 eV. Comparison of our prediction with these results indicates that the brittle crack propagation requires a lower energy barrier than the dislocation/TB reaction in nanotwinned Cu.

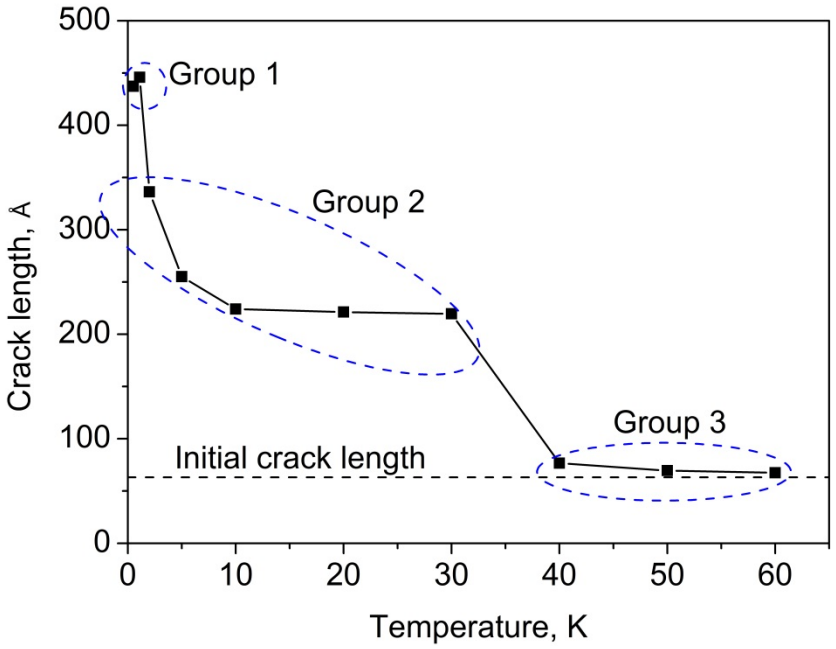

Fig. 7 Crack length at ε = 3% for different temperatures.

The crack lengths at a strain of 3% have been plotted against the temperatures in Fig. 7. The cases at 0.5 K and 1.1 K have longer cracks. The crack length decreases significantly as the temperature increases from 1.1 K to 2 K. Further increase of temperature leads to a near plateau from 10 K to 30 K. A second reduction in the crack length occurs between 30 K and 40 K, followed by a slight reduction as the temperature increases further. The studied simulation cases can be categorised into three groups according to their fracture behaviour shown in Fig. 7. In Group 1 the fracture propagates in a brittle mode during the entire simulation period. In Group 2 the fracture exhibits a dynamic brittle-to-ductile transition, while in Group 3 the ductile fracture dominates even though a short brittle fracture period appears soon after the fracture initiates. Fig 4 clearly indicates that brittle fracture is controlled by a sequential bond breaking process. The cases at 10 K and 40 K are chosen to further understand the fracture mechanisms in Group 2 and Group 3 respectively.

3.4 Dislocation activity

Fig. 8 shows the activities of dislocations radiating from the crack tip at 10 K. In Fig 8(a), the envelope of the crack is represented by a grey-coloured surface. The simulation cell is observed from the top-right-front direction. The TBs are highlighted in red. At the imposed strain of 2.751% (Fig. 8(a)), the crack still propagates in a brittle mode. The envelope of the crack is smooth and the crack tip is sharp. No defect is observed around the crack tip. As the imposed strain increases to 2.764% (see Fig. 8(b)), a new coherent twin boundary, parallel to the envelope surface of the crack tip, is generated below the crack tip. The crack tip becomes blunt in Fig. 8(b). The newly formed TB is narrow in the X direction and spreads along the Z direction and does not extend during the subsequent deformation.

In the following, the subscript 'M' of a dislocation Burgers vector, a crystallographic plane or a stacking fault normal indicates the Miller index of the matrix crystal. The subscript 'T' indicates the Miller index of the twinned crystal. In Fig. 8(c), representative of $\varepsilon = 2.767\%$, a perfect dislocation with the Burgers vector of $1/2[1\bar{1}0]_{\mathrm{M}}$ is seen to emit from the crack tip and travel on the $(001)_{\mathrm{M}}$ plane. The perfect dislocation is represented in the figure by a green tube. Previous studies [17, 18, 38] reported that Shockley partial dislocations can be emitted from the crack tip in Cu. However, the release of a perfect dislocation on the (001) plane has not been reported to date. The $1/2[1\bar{1}0]_{\mathrm{M}}$ perfect dislocation continues to travel on the (001) plane as the strain reaches 2.78% (Fig. 8(d)). The Burgers vectors of dislocations and the normal vectors of the stacking faults are marked by white and yellow symbols in the figure. It can be seen that this perfect dislocation is curved, indicating that it is a combination of edge dislocation and screw dislocation. When the $1/2[1\bar{1}0]_{\mathrm{M}}$ perfect dislocation moves, a $1/6[1\bar{1}2]_{\mathrm{M}}$ Shockley partial dislocation loop is generated on the $(\bar{1}11)_{\mathrm{M}}$ plane above the travelling $1/2[1\bar{1}0]_{\mathrm{M}}$ perfect dislocation, as shown in Fig. 8(d). It should be noted that the $1/6[1\bar{1}2]_{\mathrm{M}}$ Shockley partial dislocation loop was not emitted from the crack tip but inside the M_4 crystal. In addition, a leading $1/6[2\bar{1}1]_{\mathrm{M}}$ Shockley partial dislocation, followed by a

trailing $1/6[1\bar{2}\bar{1}]_{\mathrm{M}}$ Shockley partial dislocation (not shown in Fig. 8(d)), is released from the crack tip.

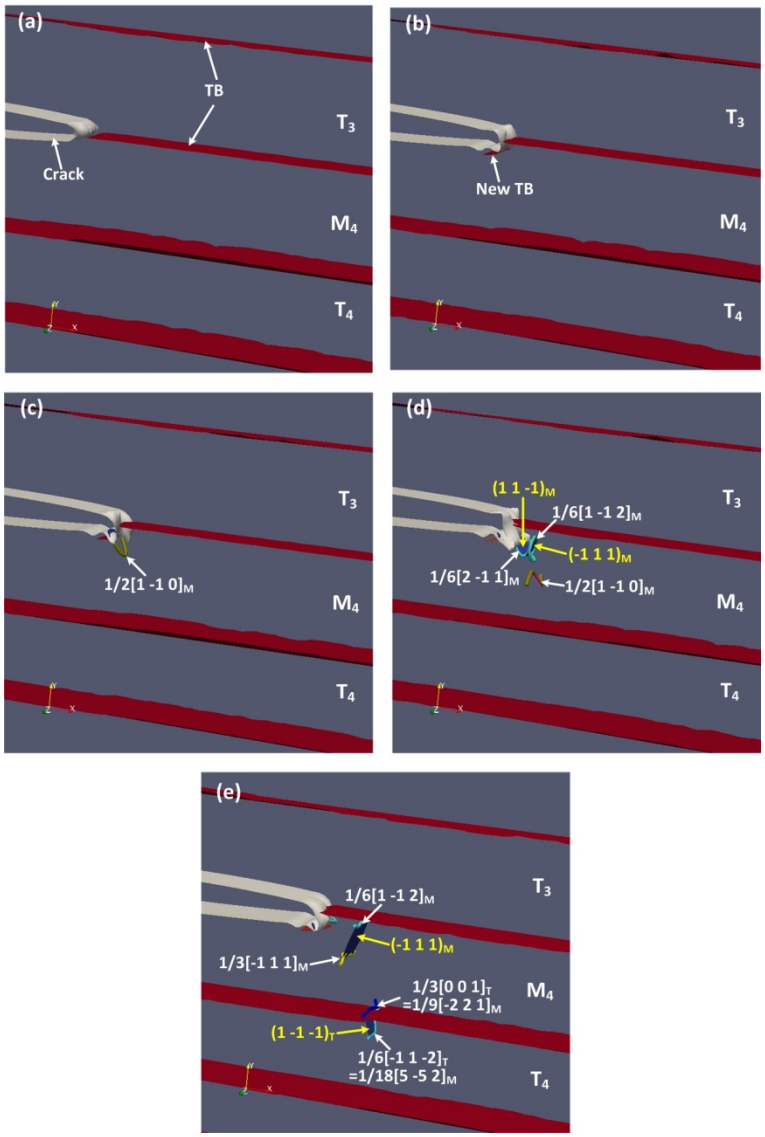

Fig. 8 Dislocation activities around the crack tip for the 10 K case: (a) ε = 2.751%; (b) ε = 2.764%; (c) ε = 2.767%; (d) ε = 2.78%; (e) ε = 2.793%.

In Fig. 8(e), the $1/6[1\bar{1}2]_{\mathrm{M}}$ Shockley partial dislocation loop expands, enveloping an intrinsic stacking fault with the normal vector of $(\bar{1}11)_{\mathrm{M}}$. As it meets the front and rear boundary surfaces of the simulation cell the dislocation loop separates into two dislocation lines with the same Burgers vector connected by the $(\bar{1}11)_{\mathrm{M}}$ stacking fault. The top $1/$

$6[1\bar{1}2]_M$ dislocation line propagates towards the TB between the T_3 crystal and the M_4 crystal. The bottom $1/6[1\bar{1}2]_M$ dislocation line soon reacts with the $1/6[2\bar{1}1]_M$ leading and $1/6[1\bar{2}\bar{1}]_M$ trailing partial dislocations emitted from the crack tip. The reaction results in a $1/3[1\bar{1}\bar{1}]_M$ Frank partial dislocation as marked in Fig. 8(e). The $1/3[1\bar{1}\bar{1}]_M$ Frank partial dislocation and the top $1/6[1\bar{1}2]_M$ dislocation are connected by the $(\bar{1}11)_M$ stacking fault. Since the Frank partial dislocation is sessile, it pins the $(\bar{1}11)_M$ stacking fault to prevent the stacking fault from shrinkage.

It is also seen in Fig. 8(e) that the first released $1/2[1\bar{1}0]_M$ perfect dislocation cuts through the TB between the M_4 crystal and the T_4 crystal. The reaction between the dislocation and the TB results in a step at the twin boundary. $1/2[1\bar{1}0]_M$ dissolves into two dislocations in the Miller index of the M_4 crystal: $1/9[\bar{2}21]_M$ and $1/18[5\bar{5}2]_M$. In the Miller index of the twinned crystal these two dislocations are $1/3[001]_T$ and $1/6[\bar{1}1\bar{2}]_T$, respectively. $1/9[\bar{2}21]_M = 1/3[001]_T$ is sessile in both crystals. Therefore, it will stay at the TB. $1/6[\bar{1}1\bar{2}]_T$ is glissile in the twinned crystal (T_4). It moves on the $(1\bar{1}\bar{1})_T$ plane in the T_4 crystal, dragging an intrinsic stacking fault.

Fig. 9 shows the dislocation activities around the crack tip at 40 K. The simulation cell is observed from the top-right-front direction. In Fig. 9(a) the imposed strain is 2.52%, a condition at which the crack just starts to propagate in a brittle mode along the TB. The crack envelope is quite smooth. Soon afterwards ledges appear on the crack tip as shown in Fig. 9(b). When the strain increases to 2.559% (Fig. 9(c)) a V-shape defect structure is emitted around the ledges into the twinned crystal (T_3), which is constructed with two intrinsic stacking faults with the normals of $(\bar{1}\bar{1}1)_T$ and $(111)_T$, respectively. These two intrinsic stacking faults are bounded by leading $1/6[\bar{2}1\bar{1}]_T$ and $1/6[1\bar{2}1]_T$ Shockley partial dislocations and they intersect at a $1/6[\bar{1}\bar{1}0]_T$ stair-rod dislocation. It has been reported that

such V-shape defect structure can nucleate from a grain boundary in nanocrystalline palladium [39].

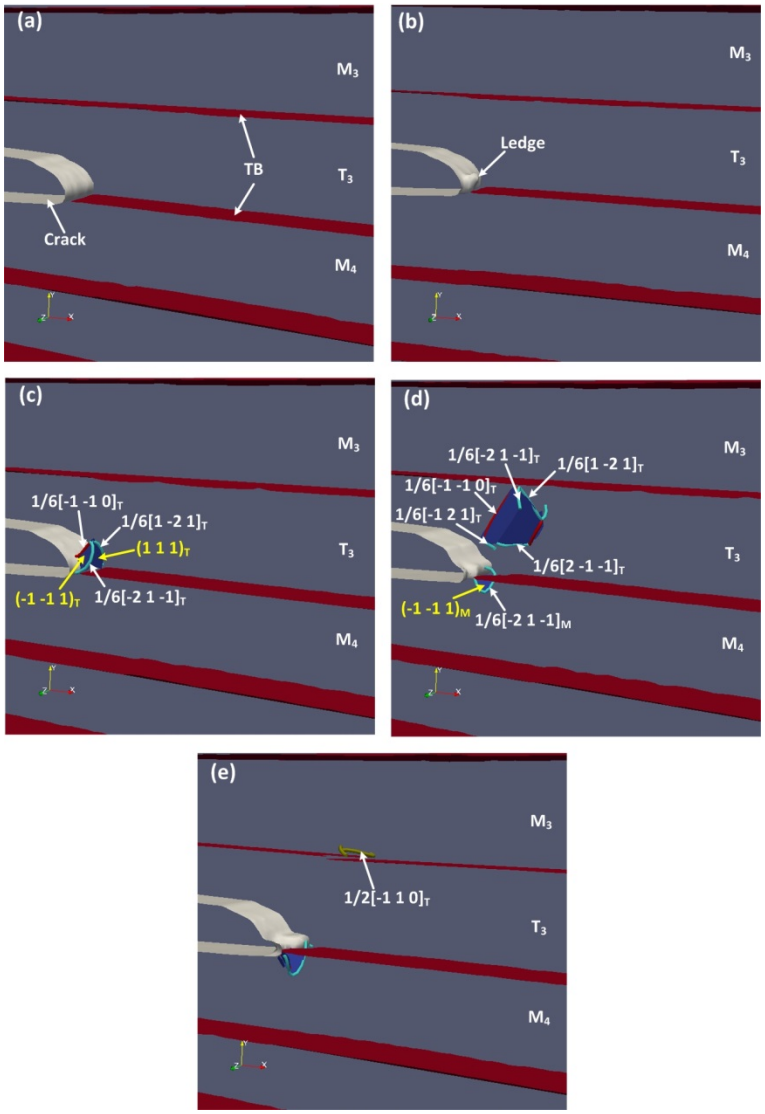

Fig. 9 Dislocation activities around the crack tip for the 40 K case: (a) ε = 2.52%; (b) ε = 2.537%; (c) ε = 2.559%; (d) ε = 2.59%; (e) ε = 2.604%.

In Fig. 9(d), representative of ε = 2.59%, the V-shape defect structure evolves into a Z-shape defect structure due to the periodic boundary condition imposed in the Z direction. The leading partial dislocations head towards the TB between the M_3 crystal and the T_3 crystal. The corresponding trailing partial dislocations ($1/6[\bar{1}21]_T$ and $1/6[2\bar{1}\bar{1}]_T$) are released from the crack tip. A new Shockley partial dislocation ($1/6[\bar{2}1\bar{1}]_M$), bounding an intrinsic

stacking fault, is emitted from the crack tip into the matrix lattice (M_4). The partial dislocation then evolves to another V-shape defect structure in Fig. 9(e). As observed in Fig. 9(e), the leading partials and trailing partials in the T_3 crystal merge into a $1/2[\bar{1}10]_T$ perfect dislocation at the TB between the M_3 crystal and the T_3 crystal.

4. Discussion

The MD simulation results indicate that different types of dislocations can be emitted from the crack tip at different temperatures in nanotwinned Cu, leading to brittle-to-ductile transition. In the following paragraphs, we discuss the atomic mechanism responsible for the dislocation nucleation.

4.1 Phase transformation

The simulation cell in this study has a two-layer (110) stacking sequence along the Z direction. Figs. 10(a1-a5) show atomic configurations around the crack tip for two successive (110) planes. These planes are initially located at Z = 11.505 Å and Z = 12.786 Å. In the following, they will be referred to as the first (110) plane and the second (110) plane respectively. The Z coordinates of the atoms are colour-coded according to the colour bar in Fig. 10(a1). The first (110) plane and the second (110) plane are coloured near-blue and near-red, respectively, in Fig. 10(a1). Figs. 10(b1-b5) show the same atomic configurations as in Figs. 10(a1-a5) but they use different colouring to distinguish the local crystal structure around each atom determined by Common Neighbour Analysis (CNA) method. In the CNA method the nearest neighbours of an atom are first obtained within the cut-off distance for the presumed crystal structure. Different crystal structures have different cut-off distances. By comparing the calculated nearest neighbours for each atom with the nearest neighbours for perfect structure crystals the following crystal structures can be determined: FCC lattice, hexagonal close packed (HCP) lattice, body-centred cubic (BCC) lattice, icosahedral lattice, and unknown lattice. The atoms coloured grey and yellow in Figs. 10(b1-b5) are in the

perfect FCC structure and HCP structure, respectively. Both the TB and the intrinsic stacking fault have the HCP structure. The atoms not associated with either the FCC structure or the HCP structure are coloured black in Figs. 10(b1-b5).

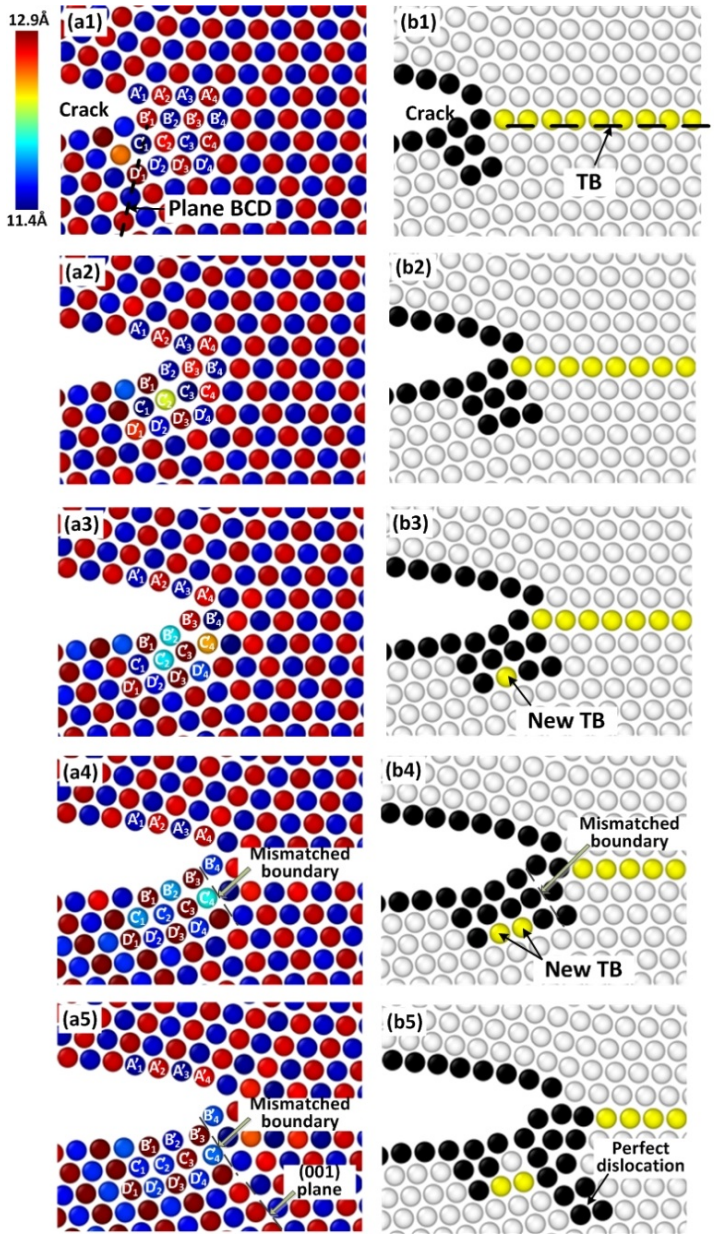

Fig. 10 Atomic configuration (a1-a5) and local crystal structure (b1-b5) around the crack tip for two successive (110) planes at different strains: (a1-b1) ε = 2.751%; (a2-b2) ε = 2.755%; (a3-b3) ε = 2.758%; (a4-b4) ε = 2.761%; (a5-b5) ε = 2.763%; in (b1-b5) the perfect FCC and HCP atoms are shown in grey and yellow, respectively, and the free surface atoms are shown in black.

Four groups of atoms have been marked in Fig. 10(a1). They are A_1'~A_4', B_1'~B_4', C_1'~C_4' and D_1'~D_4', respectively. It can be seen in Fig. 10(a1), corresponding to ε = 2.751%, that all the atoms maintain their original (110) planes. Atoms C_1', D_1' and D_2' are disordered due to the disturbance of the bond breaking process as shown in Fig. 10(b1).

As shown in Fig. 10(a1), Atoms C_1', B_2', D_2' and C_3' are initially located at the same (110) plane while Atom C_2' is located at the neighbouring (110) plane. It is interesting to note that Atom C_2' changed in colour from near-red in Fig. 10(a1) to near-green in Fig. 10(a2), indicating that this atom moves from the second (110) plane toward the first (110) plane along the plane normal. That is, C_2' attempts to squeeze into the space between Atom B_2' and Atom D_2'. This results in the fact that five atoms C_1', B_2', C_2', D_2' and C_3' are roughly located at the same plane. A careful inspection indicates that a base-centred orthorhombic structure has been locally formed with lattice constants a = 2.326 Å, b = 4.270 Å and c = 2.556 Å. Once the $A_2' - B_2'$ bond breaks, the stretching between B_2' and D_2' stops and Atom B_2' springs back toward Atom D_2'. This makes the new phase structure unstable and one of its constitutive atoms C_3' jumps from the first (110) plane to the (110) plane above it, which is equivalent to the second (110) plane, along the positive Z direction. A C_3'-type atom then moves into the space between Atom B_3' and Atom D_3' as shown in Fig. 10(a3). The consequence of these activities is that a twin boundary (TB) is generated at Atom D_3', as shown in Fig. 10(b3). Following the same mechanism, as the imposed strain increases to 2.761%, the newly formed TB is extended by an atomic distance as observed in Fig. 10(b4). However, the newly formed TB shields the atom at the crack tip and impedes the increase of its stresses. This arrests the bond breaking process. In turn the expansion of the newly formed TB no longer continues. It can be seen in Fig. 10(b4) that Atoms B_2', C_2', B_3', C_3' and C_4' make up a new twinned region relative to the M_4 crystal. This new twinned region has a mismatched boundary with the M_4 crystal, as marked in Fig. 10(a4) and Fig. 10(b4). The mismatched boundary is a weak link,

where sliding can occur easily under straining. It can be seen in Figs. 10(a5) and 10(b5) that the mismatched boundary coincides with the (001) plane of the M_4 crystal. Therefore, as the imposed strain increases the relative movement at the mismatched boundary can trigger the nucleation of a $1/2[1\bar{1}0]$ perfect dislocation on the (001) plane, which leads to the observation in Fig. 8(c).

Hai and Tadmor [40] observed deformation twinning at the crack tip of aluminium using a mixed continuum and atomistic approach. In their simulation, the first partial dislocation was emitted from the crack tip and travelled on the plane intersecting the crack tip, leaving an intrinsic stacking fault in its wake. Subsequently, a second partial dislocation was emitted on the plane adjacent and behind the previous emission plane, laying down an extrinsic stacking fault and resulting in the formation of a microtwin. The twin boundary observed in Hai and Tadmor's simulation was inclined towards the crack propagation surface. They suggested that twinning occurs when the direction of the maximum resolved shear stress coincides with the Burgers vector of a partial dislocation. The twinning mechanism observed in our study is different to that reported by Hai and Tadmor [40]. Here twinning is triggered by phase transformation and its formation can nucleate a $1/2[1\bar{1}0]$ perfect dislocation on the (001) plane.

4.2 Atomic mechanism for dynamic brittle-to-ductile transition

At 10 K, phase transformation occurred around the crack tip and induced the formation of a twinned region that nucleates a perfect dislocation. To understand the reason for phase transformation, two groups of atoms are considered. Group-B consists of all the atoms initially located at the TB between T_3 and M_4, including Atoms B_1', B_2', B_3' and B_4' marked in Fig. 10(a1). Group-D consists of all the atoms initially located at the second plane below the TB between T_3 and M_4 including Atoms D_1', D_2', D_3' and D_4'. The maximum distance (d_{BD}^{max}) between Group-B atoms and Group-D atoms always occurs near the crack tip. Fig. 11 shows

d_{BD}^{max} as a function of the imposed strain for three temperatures (1.1 K, 2 K and 10 K). It can be seen that the temperature affects d_{BD}^{max} after the strain exceeds 2.6%. At 1.1 K, d_{BD}^{max} slowly increases with the strain. In comparison, the increase in d_{BD}^{max} with the strain is faster at 2 K. d_{BD}^{max} becomes higher when the temperature increases to 10 K. Phase transformation occurs when d_{BD}^{max} reaches about 5.4 Å at both 2 K and 10 K. However, d_{BD}^{max} never reaches this critical value in the present simulation of 1.1 K. It is concluded that there is a critical distance between Group-B atoms and Group-D atoms for phase transformation to occur. When the distance between Group-B and Group-D atoms increases, the space between the two groups widens. This results in a large attractive force between the atoms at the periphery of the enlarged region. When the space between Group-B atoms (such as B_2' in Fig. 10(a2)) and Group-D atoms (such as D_2' in Fig. 10(a2)) is large enough, the attractive force will assist atoms (such as C_2' in Fig. 10(a2)) located between Group-B atoms and Group-D atoms to overcome the energy barrier to fill in the space, resulting in a phase transformation from the FCC structure to the base-centred orthorhombic structure.

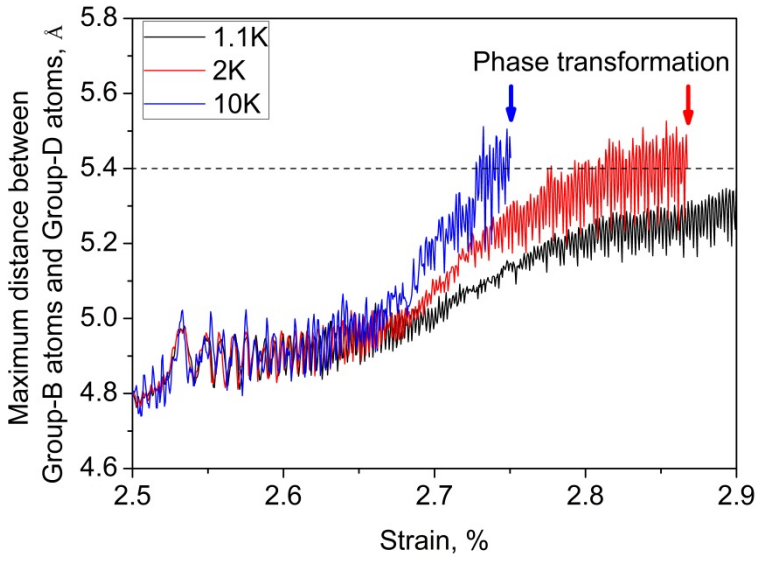

Fig. 11 Maximum distance (d_{BD}^{max}) between Group-B atoms and Group-D atoms as a function of the imposed strain.

A plane passing through a Group-B atom and its corresponding Group-D atom and parallel to the Z axis is named Plane BCD, as shown in Fig. 10(a1). The angle (θ_{BCD}) between Plane BCD and the X axis is plotted against the imposed strain in Fig. 12. θ_{BCD} generally increases with the imposed strain. As the crack propagates, the stress of most of the atoms located on the left-hand side of the crack tip is released. The stress release region is shown schematically in Fig. 4(c). The stress release in this region will cause the lattice to expand along the X direction. However, the lattice on the right-hand side of the crack is still subjected to shrinking along the X direction due to the imposed strain along the Y direction. This rotates Plane BCD slightly to a higher θ_{BCD} value as the crack propagates. When the temperature increases, thermal expansion also promotes the rotation of Plane BCD. It can be seen in Fig. 12 that θ_{BCD} increases with increasing temperature once the strain becomes larger than about 2.6%. The increased θ_{BCD} at higher temperature assists Group-B atoms at the crack tip (such as B_2' in Fig. 10(a2)) to move toward the crack opening (left-hand side of the simulation cell). This atomic flow provides more stretching space between Group-B atoms and Group-D atoms (B_2' and D_2' in Fig. 10(a2)). This is accompanied by an increase in d_{BD}^{max}. Therefore, d_{BD}^{max} reaches the critical value earlier at higher temperatures, causing phase transformation at a lower strain. Hence, the dynamic brittle-to-ductile transition occurs earlier at 10 K than at 2 K, as observed in Fig. 6. At 1.1 K, θ_{BCD} increases slowly with increasing strain. It does not reach the critical maximum distance at the end of the simulation; no dynamic brittle-to-ductile transition could be observed in this case.

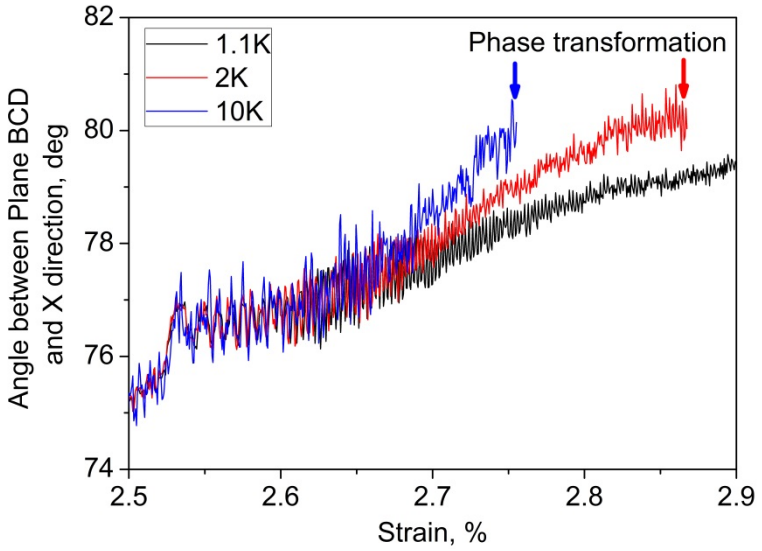

Fig. 12 Angle (θ_{BCD}) between Plane BCD and the X direction as a function of the imposed strain.

Abraham and Broughton [15] also observed dynamic brittle-to-ductile transition in their MD simulation of notched FCC solids using simple interatomic potentials. They attributed the reason of this phenomenon to a dynamic instability of brittle fracture. In this study we find that the local atomic space around the crack tip can increase during the brittle crack propagation in nanotwinned Cu at temperatures between 2 K and 30 K. When the space exceeds a certain level, a phase transformation occurs. This forms a new twinned region and nucleates a perfect dislocation on the (001) plane. The formation of the twinned region and the emission of the dislocation shield the crack tip and lower the stress at the crack tip, which results in the transition of the crack propagation from a brittle mode to a ductile mode.

4.3 Atomic mechanism for ductile fracture

In Fig. 9, the case at 40 K indicates that ledges are first formed on the crack tip, followed by nucleation of dislocations around the ledges. It is interesting to know why the ledge was generated. Fig. 13(a) shows two successive $(\bar{1}\bar{1}0)$ planes within the Z range of 11.3 Å $\leq$ Z $\leq$ 13 Å at the strain of 2.529%. Fig. 13(b) displays two successive $(\bar{1}\bar{1}0)$ planes within the Z

range of 17.7 Å ≤ Z ≤ 19.3 Å at the same strain. The atoms in Fig. 13 are coloured according to their stress along the Y direction (σ_y). Six atoms have been marked in the figures. Atoms $B_1^{"}$ and $B_2^{"}$ are initially located at the TB between the T_3 crystal and the M_4 crystal. Atoms $A_1^{"}$ and $A_2^{"}$ are initially located at the first $(1\bar{1}1)$ plane above the TB. Atoms $E_1^{"}$ and $E_2^{"}$ are at the second $(1\bar{1}1)$ plane above the TB. It can be seen in Fig. 13(a) that the bond rupture occurs between Atom $B_1^{"}$ and Atom $A_1^{"}$ for 11.3 Å ≤ Z ≤ 13 Å. However, when the observation domain moves to 17.7 Å ≤ Z ≤ 19.3 Å, as shown in Fig. 13(b), the atomic bond breaks between Atom $E_1^{"}$ and Atom $A_1^{"}$. The thermal fluctuation of Atom $A_1^{"}$ could cause variations in the $E_1^{"}$-$A_1^{"}$ and $B_1^{"}$-$A_1^{"}$distances. At lower temperature, the $B_1^{"}$-$A_1^{"}$distance is always greater than the $E_1^{"}$-$A_1^{"}$ distance. Therefore, the atomic bond breaking always occurs between the $A_1^{"}$-$A_2^{"}$ plane and the $B_1^{"}$-$B_2^{"}$ plane at lower temperatures. However, higher temperatures may significantly increase the $E_1^{"}$-$A_1^{"}$ distance. When the $E_1^{"}$-$A_1^{"}$ distance exceeds a critical value, the atomic bond breaking will occur between the $E_1^{"}$-$E_2^{"}$ plane and the $A_1^{"}$-$A_2^{"}$ plane. This means that due to the thermal influence, the crack may propagate along two adjacent crystallographic planes at different Z locations. In other words, the crack tip front is no longer straight in the Z direction. This results in ledges perpendicular to the crack propagation plane. Zhu and Thomson [9] proposed that a ledge might be formed by passing a number of screw dislocations through the crack tip on a slip plane normal to the crack line. We find an alternative mechanism for the formation of the ledge on crack: the thermal fluctuation at the higher temperature causing the crack to propagate simultaneously along different crystallographic planes, resulting in ledges on the crack tip.

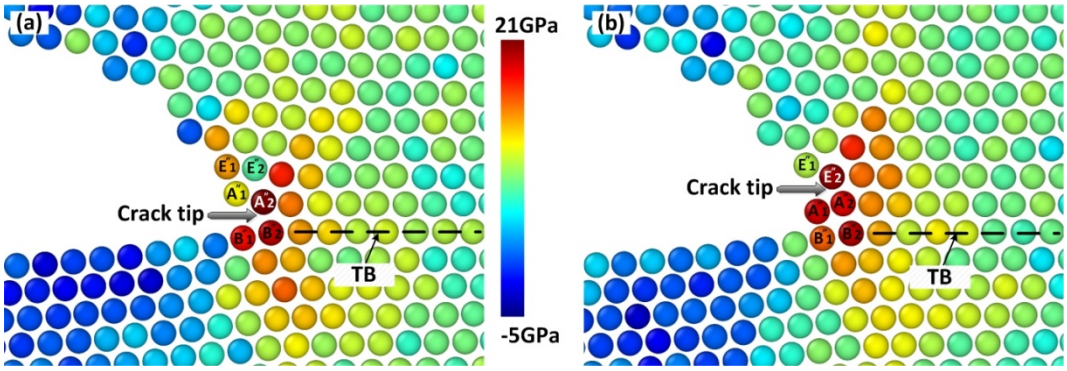

Fig. 13 Stress along the Y direction (σ_y) for the 40 K case at $\varepsilon = 2.529\%$: (a) 11.3 Å $\leq Z \leq$ 13 Å; (b) 17.7 Å $\leq Z \leq$ 19.3 Å.

5. Conclusion

In this study, MD simulations were performed to investigate the fracture behaviour in nanotwinned Cu. A through-thickness crack was generated on one side of the simulation cell with the crack surface coinciding with a twin boundary. Under tensile straining perpendicular to the twin boundary, the crack behaved in three different manners at different temperatures. The major observations can be summarised as follows:

1) At temperature up to 1.1 K, the crack propagates in a brittle fashion. Atomic bond breaking is responsible for the brittle fracture behaviour.
2) From about 2 K to about 30 K, a dynamic brittle-to-ductile transition was observed. The fracture propagates in a brittle mode before it changes to a ductile mode when the imposed strain reaches a critical level. It was found that the local inter-atomic spacing around the crack tip can increase during the brittle crack propagation as the temperature increases and/or the brittle crack propagates. When the spacing exceeds a certain level, a phase transformation occurs, which can induce the formation of a new twinned region around the crack tip and nucleates a perfect dislocation on the (001) plane. The formation of the twinned region and the emission of the dislocation shield

the crack tip and lower the stress at the crack tip. This results in the transition from a brittle mode to a ductile mode.

3) The crack propagates in a ductile mode as the temperature is raised above 40 K. In this regime the crack can propagate along two adjacent crystallographic planes due to thermal activation of atoms at the crack tip. This results in the jogged crack tip front with ledges perpendicular to the crack propagation plane, followed by emission of the dislocations around the ledges. The latter activity shields the atoms around the crack tip and impedes brittle crack propagation.

Acknowledgement

L.P., X.Z. and L.Z. acknowledge support from the China scholarship council. Access to the supercomputer facilities provided by the University of Wollongong and the National Facility of the National Computational Infrastructure of Australia is also acknowledged.

References

[1] Gumbsch P, Riedle J, Hartmaier A, Fischmeister HF. Science 1998;282:1293.

[2] Khantha M, Pope DP, Vitek V. Phys Rev Lett 1994;73:684.

[3] Rice JR, Thomson R. Phil Mag 1974;29:73.

[4] Hirsch PB, Roberts SG. Acta Mater 1996;44:2361.

[5] Rice JR. J Mech Phys Solids 1992;40:239.

[6] Argon AS, Maloof SR. Acta Metall Mater 1966;14:1463.

[7] Anderson PM, Rice JR. Scripta Metall Mater 1986;20:1467.

[8] Li JCM. Scripta Metall Mater 1986;20:1477.

[9] Zhou SJ, Thomson R. J Mater Res 1991;6:639.

[10] Freund LB, Hutchinson JW. J Mech Phys Solids 1985;33:169.

[11] Argon AS. Acta Metall Mater 1987;35:185.

[12] Knap J, Sieradzki K. Phys Rev Lett 1999;82:1700.

[13] Cleri F, Yip S, Wolf D, Phillpot SR. Phys Rev Lett 1997;79:1309.

[14] Abraham FF, Gao H. Phil Mag Lett 1998;78:307.

[15] Abraham FF, Broughton JQ. Comp Mater Sci 1998;10:1.

[16] Zhang YW, Wang TC, Tang QH. Scripta Metall Mater 1995;33:267.

[17] Kimizuka H, Kaburaki H, Shimizu F, Li J. J Comput-aided Mater 2003;10:143.

[18] Cui CB, Beom HG. Mater Sci Eng A 2014;609:102.

[19] Lu K, Lu L, Suresh S. Science 2009;324:349.

[20] Lu L, Chen X, Huang X, Lu K. Science 2009;323:607.

[21] Jang D, Li X, Gao H, Greer JR. Nat Nanotechnol 2012;7:594.

[22] Zhu L, Ruan H, Li X, Dao M, Gao H, Lu J. Acta Mater 2011;59:5544.

[23] Zhu T, Li J, Samanta A, Kim HG, Suresh S. Proc Natl Acad Sci USA 2007;104:3031.

[24] You Z, Li X, Gui L, Lu Q, Zhu T, Gao H, Lu L. Acta Mater 2013;61:217.

[25] Plimpton S. J Comput Phys 1995;117:1.

[26] Mishin Y, Mehl MJ, Papaconstantopoulos DA, Voter AF, Kress JD. Phys Rev B 2001;63:2241061.

[27] Stukowski A. Model Simul Mater Sci Eng 2010;18:015012.

[28] Stukowski A, Bulatov VV, Arsenlis A. Model Simul Mater Sci Eng 2012;20:085007.

[29] Stukowski A, Albe K. Model Simul Mater Sci Eng 2010;18:085001.

[30] Meyers MA, Chawla KK. Mechanical Behavior of Materials. Cambridge University Press;2009.

[31] Freund LB. Dynamic Fracture Mechanics. New York: Cambridge University Press;1990.

[32] Gao H, Huang Y, Abraham FF. J Mech Phys Solids 2001;49:2113.

[33] Ledbetter HM, Naimon ER. J Phys Chem Ref Data 1974;3:897.

[34] Fineberg J, Gross S, Marder M, Swinney H. Phys Rev Lett 1991;67:457.

[35] Bergkvist H. Eng Fract Mech1974;6:621.

[36] Zhou SJ, Lomdahl PS, Thomson R, Holian BL. Phys Rev Lett 1996;76:2318.

[37] Glasstone S, Laidler K, Eyring H. The Theory of Rate Processes. New York: McGraw Hill;1941.

[38] deCelis B, Argon AS, Yip S. J Appl Phys 1983;54:4864.

[39] Stukowski A, Albe K, Farkas D. Phys Rev B 2010;82:224103.

[40] Hai S, Tadmor EB. Acta Mater 2003;51:117.